J. Fluid Mech. (1995), *vol.* 300, *pp.* 311–338

Symmetry, sidewalls, and the transition to chaos in baroclinic systems

By MICHAEL D. MUNDT[1]†, JOHN E. HART[1, 2] AND DANIEL R. OHLSEN[1]

[1]Program in Atmospheric and Oceanic Sciences, Box 311, University of Colorado, Boulder, CO 80309, USA

[2]Department of Astrophysical, Planetary, and Atmospheric Sciences, Box 391, University of Colorado, Boulder, CO 80309, USA

(Received 20 January 1995 and in revised form 5 June 1995)

A high-resolution, quasi-geostrophic numerical model is utilized to examine two-layer baroclinic flow in a cylinder. Particular attention is given to the role of horizontal shear of the basic state induced by viscosity near the cylinder wall, and to the desymmetrization brought about by the cylindrical geometry, in the transition to baroclinic chaos. Solutions are computed for both f-plane and β-plane situations, and the results are compared to previous laboratory experiments. Agreement in the former case is found to be good, although the onset of chaos occurs at slightly lower forcing in the laboratory when its basic flow is prograde, and at higher forcing amplitude when the experimental basic azimuthal currents are retrograde. This suggests that the modest discrepancies may be attributable to computationally neglected ageostrophic effects in the interior fluid and Ekman boundary layers. When $\beta \neq 0$, the numerical and laboratory results are in excellent agreement. The computational simulations indicate that the viscous sidewall boundary layer plays a pivotal role in the dynamics. Moreover, in contrast to previous studies performed in a periodic, rectilinear channel, the route to chaos is largely temporal and involves relatively few spatial modes. The reduction in symmetries upon going from f-plane channel to either f-plane or β-plane cylinder models leads to fewer secondary instabilities and fewer spatial modes that are active in the dynamics.

1. Introduction

In a series of studies, we have tried to discover the physical processes responsible for the transition to chaos observed in laboratory experiments on finite-amplitude baroclinic instability. The experiments on two-layer flows on the f-plane (Hart 1972, 1985) and β-plane (Ohlsen & Hart 1989*a*,*b*) exhibit a panoply of dynamical behaviour, including steady flow, various types of periodic vacillations and chaos. Moreover, the onset of aperiodic flow occurs when the system is only moderately unstable ($\Delta \approx 1$) to wavelike disturbances, indicating that chaos is quite easy to induce. The supercriticality Δ is here defined as $\Delta \equiv (F - F_c)/F_c$, where F is the rotational Froude number and F_c is the critical value of F needed for instability.

Comparisons of low- or moderate-order models (e.g. those of Pedlosky & Frenzen

† Present address: Institute of Marine Science, University of California at Santa Cruz, Santa Cruz, CA 95064, USA.

1980; Hart 1986; Yoshida & Hart 1986; Ohlsen & Hart 1989*b*) with laboratory experiments have met with only modest success. For example, the onset of periodic and chaotic behaviour in the models generally does not coincide with that observed in the laboratory. There are two factors that apparently contribute to the discrepancy between model and experimental results. First, in some of the models a zonally periodic channel geometry is used. The experiments, however, are conducted in a cylinder. Second, all of the low-order models ignore the viscous effects near the no-slip sidewall(s), preferring instead to neglect lateral friction altogether for simplicity of analysis.

Recently, efforts have been made to construct high-resolution models of two-layer, quasi-geostrophic flow which presumably exhibit more realistic behaviour at larger supercriticality. Klein & Pedlosky (1986), Cattaneo & Hart (1990), and Mundt and Hart (1994) considered high-resolution models in a free-slip channel geometry with up to 128×65 modes in each layer. While exhibiting complex spatio-temporal motions, the numerical findings were nonetheless still disappointing when compared to experimental results. While the onset of chaos in the laboratory occurs at about unit supercriticality, in these numerical models it is deferred to $\Delta \approx 4$. In an attempt to rectify this major discrepancy, Mundt, Brummell & Hart (1995) considered an f-plane channel with rigid (no-slip) sidewalls. The results were quite surprising. For thicker sidewall boundary layers (and relatively small Ekman suction), chaotic behaviour was observed to occur at or below the linear neutral curve as a result of subcritical bifurcations. For thinner sidewall layers, chaos arose through a supercritical quasi-periodic bifurcation when $\Delta \approx 1$. The inviscid interaction of the baroclinic waves with the horizontal shear induced by viscosity near the sidewalls is destabilizing, and it can completely overcome the stabilizing influence of interfacial friction, which previously had expunged the strange attractors in the free-slip simulations.

Although the inclusion of rigid sidewalls brings the critical point for transition to chaos into qualitative agreement with experimental results, quantitative correspondence is still lacking. For instance, both f-plane and β-plane laboratory experiments exhibit period-doubling routes to chaos. In addition, there are complex periodic states on the β-plane, such as nonlinear interference vacillation (Ohlsen & Hart 1989*b*), which depend on the forcing direction in the experiments, but not in intermediate models. In both the free-slip and no-slip channel models, it has been noted that symmetry breaking plays a prominent role in the transition to chaos (Mundt & Hart 1994; Mundt *et al.* 1995). Temporal bifurcations (e.g. steady to periodic, periodic to quasi-periodic) are accompanied by a breaking of one or more spatial symmetries, which are described in §2. Since these particular symmetries do not exist in the cylinder, we hypothesize that they influence the type of transition sequence one obtains, as well as the dimension of the resulting chaos.

In order to examine the effects of a realistic geometry coupled with a viscous sidewall, we have formulated a high-resolution model of two-layer flow in a rigid-wall cylinder. We consider both f-plane and β-plane motions, to provide a comprehensive comparison with laboratory results. One objective is to ascertain the degree to which the observed experimental behaviour, which occurs at small to moderate Rossby numbers, can be described by the quasi-geostrophic equations. Another is to determine the role of geometrical symmetries and spontaneous symmetry breaking in the transition to chaos.

The paper is organized as follows. Section 2 introduces the governing equations, lists the important parameters, and describes the important symmetries of the systems. The basic-state solution for a rigid cylinder is derived in §3. In §4 we present linear stability diagrams, and the results are compared with experiment and previous

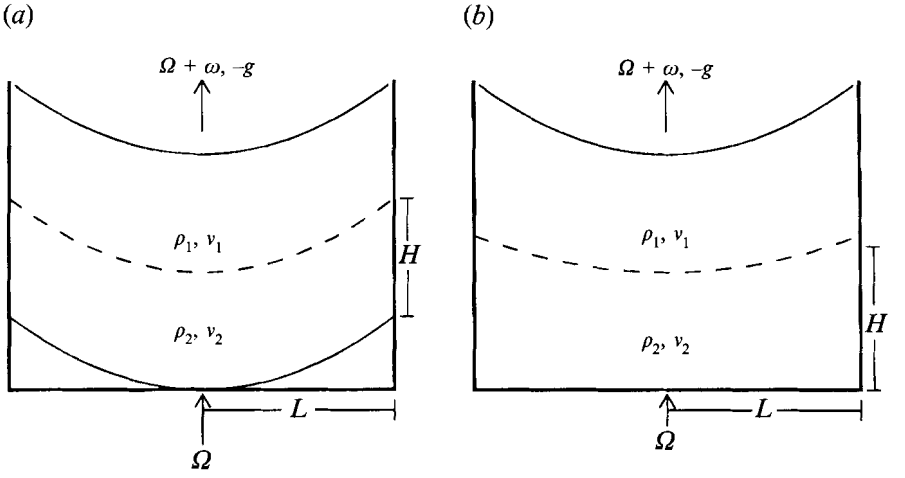

FIGURE 1. Schematic of (*a*) *f*-plane and (*b*) β-plane geometries. In the *f*-plane configuration, the top and bottom surfaces are aligned with the fluid interface. In the β-plane geometry, the curvature of the top lid is twice that of the interface, while the bottom is flat.

stability calculations. In §5 the numerical method is outlined, and then results for both *f*-plane and β-plane geometries are presented. The behaviour is compared to the experimental findings, and we attempt to provide a physical explanation for the observed results. Empirical orthogonal function (EOF) analysis is utilized in §6 to diagnose the spatio-temporal complexity of the solutions and to examine the role of symmetry breaking in the transition to chaos. In §7 we present our conclusions.

2. Governing equations

The fluid is contained in a cylinder of radius L that rotates with an angular frequency Ω. The wall at $r = L$ is rigid (i.e. the velocity of the fluid is zero at the wall). The flow itself consists of two immiscible fluids, with densities ρ_i and viscosities ν_i, $i = 1, 2$. The volumes of the two layers are equal, the equilibrium depth is denoted by H, and the upper lid rotates at a differential frequency ω. The configuration is shown schematically in figure 1.

In order to simulate the *f*-plane, the curvature of the top lid and bottom tank surface is made equal to that of the interface between the two fluids when the basic rotation Ω is present (Hart 1985). Similarly, a polar β-plane can be obtained by using a flat bottom and a top lid whose curvature is twice that of the interface parabola due to Ω (Hart 1972; Ohlsen & Hart 1989*a*). Vortex columns then get stretched with increasing radial position in both layers, forming a topographic β-effect.

When the relative vorticity, measured by ω, is small compared to the planetary vorticity 2Ω, the flow may be described by the quasi-geostrophic approximation. We non-dimensionalize using L as a length scale, ω^{-1} as a time scale, and $L\omega$ as a velocity scale. For equal layer depths and a non-dimensional upper lid driving (ω_T) equal to the sign of ω (or the sign of Q, see below), the governing potential-vorticity equations for the two layers are (Hart 1972)

$$\left[\frac{\partial}{\partial t} + J(P_1, \,)\right][\nabla^2 P_1 + F(P_2 - P_1)] = -|Q|(\nabla^2 P_1 - 2\omega_T)$$
$$+|Q|\frac{\chi}{1+\chi}(\nabla^2 P_2 - \nabla^2 P_1) - \frac{\beta}{|Ro|}\frac{\partial P_1}{\partial \theta} + \frac{E_{L_1}}{|Ro|}\nabla^4 P_1, \qquad (2.1)$$

$$\left[\frac{\partial}{\partial t} + J(P_2,)\right][\nabla^2 P_2 - F(P_2 - P_1)] = -|Q|\chi(\nabla^2 P_2)$$
$$-|Q|\frac{\chi}{1+\chi}(\nabla^2 P_2 - \nabla^2 P_1) - \frac{\beta}{|Ro|}\frac{\partial P_2}{\partial \theta} + \frac{E_{L_2}}{|Ro|}\nabla^4 P_2. \tag{2.2}$$

In cylindrical coordinates, the Jacobian J is defined as

$$J(a,b) \equiv \frac{1}{r}\left(\frac{\partial a}{\partial r}\frac{\partial b}{\partial \theta} - \frac{\partial a}{\partial \theta}\frac{\partial b}{\partial r}\right), \tag{2.3}$$

and

$$\nabla^2 \equiv \frac{\partial^2}{\partial r^2} + \frac{1}{r}\frac{\partial}{\partial r} + \frac{1}{r^2}\frac{\partial^2}{\partial \theta^2}. \tag{2.4}$$

The parameter F is the rotational Froude number,

$$F = \frac{2\Omega^2 L^2(\rho_1 + \rho_2)}{gH(\rho_1 - \rho_2)}, \tag{2.5}$$

Ro is the Rossby number,

$$Ro = \frac{\omega}{2\Omega}, \tag{2.6}$$

χ is the viscosity ratio,

$$\chi = \left(\frac{\nu_2}{\nu_1}\right)^{1/2}, \tag{2.7}$$

E_{L_1} and E_{L_2} are the lateral Ekman numbers,

$$E_{L_1} = \frac{\nu_1}{2\Omega L^2}, \quad E_{L_2} = \frac{\nu_2}{2\Omega L^2} = \chi^2 E_{L_1}, \tag{2.8}$$

E_z is the vertical Ekman number,

$$E_z = \frac{\nu_1}{2\Omega H^2}, \tag{2.9}$$

Q is the Ekman layer friction parameter,

$$Q = \frac{(\nu_1 \Omega)^{1/2}}{H\omega} = \frac{E_z^{1/2}}{\sqrt{2}Ro}, \tag{2.10}$$

and β is the 'planetary vorticity gradient' caused by topographic stretching,

$$\beta = (\Delta d)/H, \tag{2.11}$$

where Δd is the total height variation of the lid parabola.

In the laboratory, the parameters are generally fixed by the geometry and the properties of the fluids in the two layers. The Froude number is changed by altering the density of the fluid in one of the layers. Experiments are usually carried out by fixing F and changing ω to alter Q. We mimic this procedure in most of the numerical runs for easier comparisons to laboratory results.

The velocities in the two layers are evaluated geostrophically and are given by

$$u_k = -\frac{1}{r}\frac{\partial P_k}{\partial \theta}, \quad v_k = \frac{\partial P_k}{\partial r}, \quad k = 1,2, \tag{2.12}$$

where k denotes the layer and u_k and v_k are the radial and azimuthal velocities in

the kth layer, respectively. P_k is thus the streamfunction in each layer. In later sections we also use a barotropic/baroclinic streamfunction notation. The barotropic, or depth-averaged, streamfunction can be defined by

$$P_{bt} \equiv P_1 + P_2, \tag{2.13}$$

while the baroclinic, or depth-varying, component is

$$P_{bc} \equiv P_2 - P_1, \tag{2.14}$$

and the governing equations can be re-written in terms of the variables P_{bt} and P_{bc} by taking the sum and difference of (2.1), (2.2) (see Mundt & Hart 1994). The deviation h of the interface (from its parabolic equilibrium shape) is given by

$$h = RoFP_{bc}. \tag{2.15}$$

At the rigid cylinder wall ($r = 1$) we require that

$$u_1 = u_2 = 0, \tag{2.16}$$

$$v_1 = v_2 = 0. \tag{2.17}$$

We also demand regular solutions at the origin.

Since the zonally averaged flow (a function of r only) trivially satisfies $u_1 = u_2 = 0$ everywhere, an extra boundary condition is needed for this quantity. By integrating (2.1), (2.2) over the domain and demanding that the mass of the fluid in each layer be conserved, i.e.

$$\frac{\partial}{\partial t}\int_A h \, \mathrm{d}A \propto F\frac{\partial}{\partial t}\int_A (P_2 - P_1)\, \mathrm{d}A = 0, \tag{2.18}$$

we obtain another boundary condition on the zonal flow:

$$\left.\frac{\partial \bar{\omega}_1}{\partial r}\right|_{r=1} = -\frac{|Q|\omega_T}{E_1/|Ro|}, \tag{2.19}$$

$$\left.\frac{\partial \bar{\omega}_2}{\partial r}\right|_{r=1} = 0, \tag{2.20}$$

where $\omega_k \equiv \nabla^2 P_k$ is the vorticity in the kth layer and an overbar denotes a zonally averaged quantity.

The parameters were chosen to emulate the laboratory experiments of Hart (1985) and Ohlsen & Hart (1989*a*,*b*). In table 1 we list, for reference, the important dimensional and non-dimensional parameter values.

Owing to both geometry and parameter constraints, the traditional f-plane rectilinear channel model possesses several symmetries not present in the laboratory cylinder (Mundt & Hart 1994). The first symmetry, in which the basic system is recovered after exchanging the layers and changing the zonal direction ($x \to -x$), is termed flip-reverse. It occurs when $\chi = 1$, $\beta = 0$, and the basic-state velocities in the two layers are equal and opposite. In the cylindrical laboratory experiments that are forced from the top only, none of these conditions is satisfied, particularly that of equal and opposite basic flow, and the symmetry is strongly broken. Another symmetry in channel models arises from the geometry alone. Since the northern and southern halves of the channel are equivalent, there is a possible shift-reflect symmetry in the solutions. In this situation, the velocity at (x, y) is identical to the velocity at $(x + \mathscr{L}/2, 1 - y)$, where $\mathscr{L}$ is the periodicity length of the channel and the width $y \in [0, 1]$. Defining the gravest zonal (k_x) and meridional (k_y) wavenumbers to

Parameter	f-plane	β-plane
H (cm)	13.0	13.0
L (cm)	22.80	22.54
Ω (rad s^{-1})	2.856	3.465
ν_1 (cm^2 s^{-1})	0.0158	0.0158
ν_2 (cm^2 s^{-1})	0.0128	0.0143
ρ_1 (g cm^{-3})	0.851	0.851
χ	0.90	0.95
β	0	0.4792
E_1	5.324×10^{-6}	4.314×10^{-6}
E_2	4.490×10^{-6}	4.053×10^{-6}
ω	varies	varies
ρ_2	varies	varies
F	varies	varies
Q	varies	varies

TABLE 1. Summary of dimensional and non-dimensional parameter values used in f-plane and β-plane geometries.

be 1, all waves in this symmetric state have the property that $k_x + k_y$ is even, and the wavenumber set is invariant under the nonlinear operators (Cattaneo & Hart 1990). In the cylinder, however, the curvilinear coordinates destroy this symmetry. The absence of both flip-reverse and shift-reflect symmetries in the cylindrical geometry, it will be shown, has a profound effect on the observed dynamics.

3. Basic state

An exact, azimuthally invariant, steady solution of (2.1),(2.2) is

$$\bar{v}_1(r) = \left(\frac{\chi+2}{\chi+1}\right)\frac{r}{2} + c_1 I_1(\lambda_1 r) + c_2 I_1(\lambda_2 r), \tag{3.1}$$

$$\bar{v}_2(r) = \left(\frac{1}{\chi+1}\right)\frac{r}{2} + c_1\gamma_1 I_1(\lambda_1 r) + c_2\gamma_2 I_1(\lambda_2 r), \tag{3.2}$$

where the overbar again denotes an azimuthally invariant solution. The quantities λ_1, λ_2, c_1, c_2, γ_1, and γ_2 are given by algebraic relations involving χ, Q, E_{L_1}/Ro, and E_{L_2}/Ro and are listed in the Appendix. In the above equations, I_1 is a modified Bessel function of the first kind. The constants λ_1 and λ_2 are proportional to $[Q/(E_{L_1}/Ro)]^{1/2}$, yielding a boundary layer with an e-folding thickness of order $E_{L_1}^{1/4}$ (Stewartson 1957). The velocity profiles for the two layers given typical laboratory parameters of $Q = 0.1$, $\chi = 0.9$, and $E_{L_1} = 5.324 \times 10^{-6}$ (which yield $\lambda_1 = 33.8$, $\lambda_2 = 23.7$) are shown in figure 2. The interior of the flow is in solid-body rotation, while the outer wall gives rise to a viscous shear layer near $r = 1$. In contrast to the $E_{L_1} = E_{L_2} = 0$ solution, which is simply the first term on the right-hand sides of (3.1) and (3.2), the presence of the sidewall boundary layer yields large basic-state vorticities and vorticity gradients in the outer 10% of the domain.

4. Linear theory

Calculations of the onset of linear instability of single-wave disturbances in a rigid-wall, f-plane channel have been made by Mundt *et al.* (1995). They noted significant

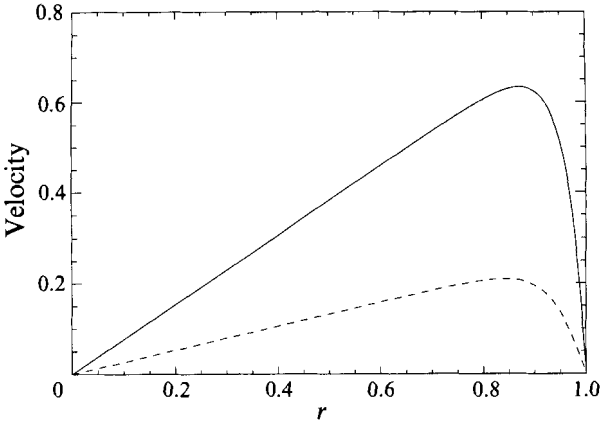

FIGURE 2. Basic-state velocity profiles for $Q = 0.1$, $\chi = 0.9$, and $E_1 = 5.324 \times 10^{-6}$. The solid and dashed lines correspond to the upper and lower layers, respectively.

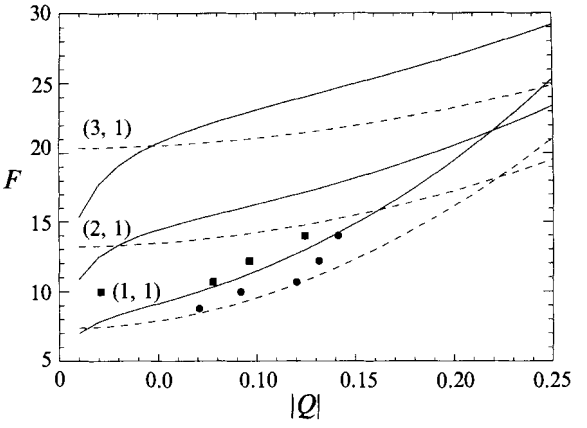

FIGURE 3. Stability curves for f-plane geometry, $\chi = 0.9$. The solid lines show the rigid-wall results, while the dashed lines show the $E_{L_i} = 0$ calculations. The circles and squares denote the onset of instability of a $k = 1$ wavy disturbance in laboratory experiments for co-rotating and counter-rotating driving, respectively. The numbers in parentheses give the wavenumber components of the corresponding $E_{L_i} = 0$ calculations.

differences when compared to results obtained using free-slip sidewalls. In particular, for a given value of Q, the critical value of F needed for instability, denoted as F_c, is a strong function of λ_1 and λ_2. As $\lambda_{1,2}$ decrease (i.e. the shear layer widens), F_c becomes larger than the free-slip value for $Q \gg 1$ but smaller for $Q \ll 1$. Large values of $\lambda_{1,2}$ with a correspondingly narrow boundary layer yield results similar to the free-slip solutions for all values of Q.

Stability curves were calculated for the rigid-sidewall cylinder by first linearizing (2.1),(2.2). The approach is similar to that described by Mundt *et al.* (1995), except that a finite-difference technique is used in this study instead of an eigenfunction expansion. Neutral curves are presented for the two sets of parameters listed in table 1. The f-plane rigid-wall neutral curves are shown in figure 3 by the solid lines, while the dashed lines show the neutral curves obtained analytically by neglecting lateral friction and requiring only that the wave normal velocity vanish at $r = 1$ (e.g. Hart 1972). The numbers in parentheses give the zonal and radial wavenumber

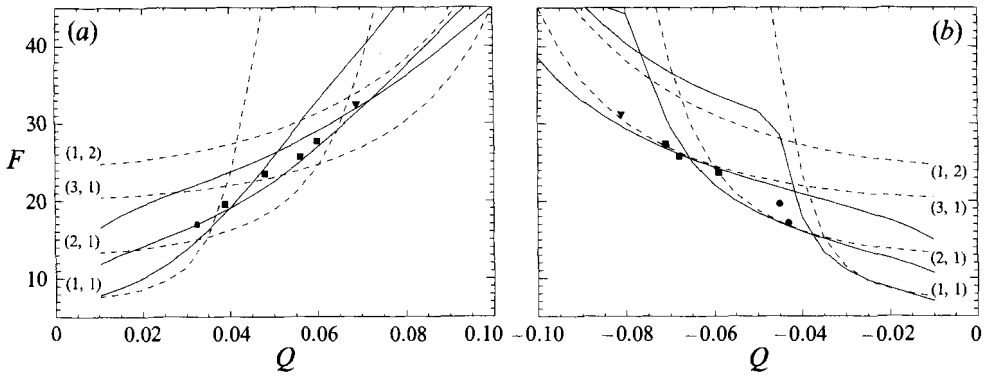

FIGURE 4. Stability curves for β-plane geometry, $\chi = 0.95$, $\beta = 0.4792$. The circles, squares, and triangles indicate the onset of $k = 1$, $k = 2$, and $k = 3$ disturbances, respectively, in the laboratory experiments. (*a*) Co-rotating case ($Q > 0$), (*b*) counter-rotating case ($Q < 0$).

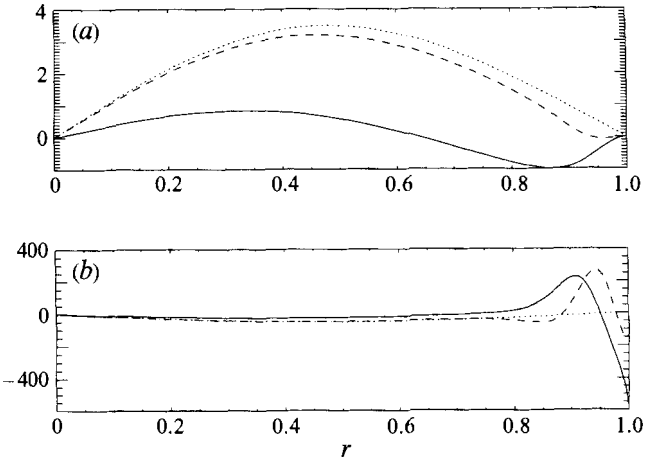

FIGURE 5. A snapshot of the upper-layer (*a*) streamfunction and (*b*) vorticity eigenfunctions for $\beta = 0$, $Q = 0.05$, $F = 9.13$, $\chi = 0.9$, and $k = 1$. The solid and dashed lines respectively show the real and imaginary parts of the eigenfunctions. The dotted line shows the $E_{L_i} = 0$ solution, proportional to $J_1(3.832r)$.

components, respectively, used in the $E_{L_i} = 0$ calculations. In the quasi-geostrophic approximation with $\beta = 0$, the behaviour of the flow is independent of the sign of the lid driving; hence the neutral curves depend only on $|Q|$. In the figure, the circles indicate the onset of instability, in this case composed of $k = 1$ disturbances, in the laboratory experiments (Hart 1985). The experimental results exhibit significant differences between co-rotating and counter-rotating lid driving. More specifically, the co-rotating results are less stable than predicted by linear theory, while the counter-rotating case is somewhat more stable. This implies that ageostrophic effects are important even when *Ro* is relatively small, although in the important lateral shear layer near $r = 1$ the local Rossby number is magnified. Note the favourable agreement with the $E_{L_i} = 0$ neutral curves for positive Q. This, in part, led to the use of models without effects of lateral friction in studying nonlinear baroclinic flows.

The β-plane results for co-rotating lid driving ($Q > 0$) are displayed in figure 4(*a*), while figure 4(*b*) shows the results for a counter-rotating lid ($Q < 0$). Also shown in the figure are the locations of the initial onset of waves, along with the dominant

wavenumber, obtained from the laboratory experiment (Ohlsen & Hart 1989*b*). The co-rotating case shows substantial differences between neutral curves calculated with $E_{L_i} = 0$ and those obtained with lateral viscosity. The agreement between the experimental results and the rigid-wall predictions are quite good. At $F \approx 16.5$, for instance, the experiment shows that $k = 1$ becomes unstable first; the rigid-wall results confirm this. The $E_{L_i} = 0$ calculations, however, indicate that the instability should be dominated by $k = 2$. For the counter-rotating case, the results are less sensitive to the sidewall boundary condition. The two sets of curves are nearly commensurate and in fact overlap for some ranges of Q. The $k = 1$ disturbance with the rigid-wall condition undergoes a transition to a higher radial mode at $Q \approx -0.05$, as in the lateral friction-free theory. For $Q < 0$, the minor discrepancies between experiment and prediction (at $F \approx 19.2$, for example, where the linear results predict $k = 2$ should become unstable first instead of the observed $k = 1$) are presumably attributable to higher-order ageostrophic effects.

The linear eigenfunctions are somewhat different from those in the $E_{L_i} = 0$ case. In the latter, the solutions are simply ordinary Bessel functions of the first kind in r (J_k for a given zonal wavenumber k). Figure 5 shows a snapshot of the real and imaginary parts (shown by solid and dashed lines, respectively) of the upper-layer streamfunction and vorticity on the f-plane for the full viscosity case just inside the stability boundary at $F = 9.13$. The real part of the streamfunction passes through zero in the interior. In addition, the vorticity at the walls is quite large, underscoring the effect of horizontal shear of the basic state induced by the no-slip condition at the sidewall. For comparison, the Bessel-function solution $J_1(\alpha r)$, $\alpha \approx 3.832$, scaled by an arbitary but similar amplitude, is shown by the dotted line. The vorticity is $-\alpha^2$ times the streamfunction solution and is very much smaller than that for the rigid-wall eigenfunctions near $r = 1$ given a comparable interior amplitude.

5. Nonlinear model

5.1. *Model formulation*

The model was formulated with a mixed pseudo-spectral/finite-difference method. A Fourier expansion was used in the azimuthal direction owing to the periodicity. In the radial direction we used finite differencing. In addition, because we anticipate much of the interesting dynamics to occur in the boundary layer near $r = 1$, and since typically the region near the origin is relatively quiescent, a stretched grid was introduced. Defining a uniform grid variable $\eta \in [0, 1]$,

$$\eta \equiv \frac{i-1}{n_r - 1}, \quad i = 1, n_r, \tag{5.1}$$

where n_r is the number of grid points used in the radial direction, the stretched grid variable ρ (which is the actual radial position of the ith grid point) is defined as

$$\rho \equiv \frac{1 - \mathrm{e}^{-\alpha\eta}}{1 - \mathrm{e}^{-\alpha}}, \tag{5.2}$$

so that $\rho \in [0, 1]$ as well. The constant α was chosen to be 2 for this study; this value provided an adequate density of points in the boundary layer (approximately 8 in an e-folding thickness for $n_r = 65$) while still resolving the interior flow.

We used a semi-implicit method in time: the linear terms were updated with a Crank–Nicholson scheme, while the nonlinear portions were marched forward with a three-level Adams–Bashforth method. The nonlinear terms were calculated by Fourier

transforming in θ and finite-differencing in r. In the azimuthal direction, a standard dealiasing scheme based on the 2/3 rule was used (Canuto *et al.* 1988).

For the zonally averaged portions of the flow, (2.17),(2.19),(2.20) were enforced explicitly. For the wavy parts, (2.16) was enforced by setting the wavy streamfunctions to 0 at $r = 1$. Equation (2.17) was satisfied implicitly by setting $\omega_k = \nabla^2 P_k$ at the sidewall, *but* assuming that $\partial P_k/\partial r = 0$ when deriving the Taylor series approximation to the vorticity in terms of the streamfunction (Anderson, Tannehill & Pletcher 1984). This approach, while not completely rigorous in satisfying (2.17) (Quartapelle & Valz-Gris, 1981), seems to yield quite satisfactory results in the sense that *a posteriori* checks indicate that $v_k = \partial P_k/\partial r$ is very nearly zero at the sidewall.

All results described in this paper were obtained with a resolution of 64×65 in the azimuthal and radial directions, respectively. Numerical runs at a resolution of 32×33 were also performed; these generally showed no substantial differences when compared to the more highly resolved computations. In a few limited cases (i.e. small values of $|Q|$), there were minor qualitative behavioural discrepancies. These appear to be attributable to a marginally resolved sidewall boundary layer in the low-resolution runs. Finally, an *a posteriori* check of the 64×65 results showed the energy possessed by the higher-wavenumber modes to be negligible.

5.2. *f-plane results*

The experimental results, obtained from Hart (1985), are displayed in figure 6 (note that in his figure 3, the abscissa needs to be multiplied by $\sqrt{2}$ to correspond to our definition). The rigid-wall neutral curves calculated in §4 have been superimposed. The figure shows results for both co-rotating and counter-rotating lid driving. Over the range of F and Q shown, the $k = 1$ wave is always the most linearly unstable. For $Q > 0$, the flow equilibrated to a steady wave state for values of Q somewhat inside the stability threshold. At smaller values of F, this steady state persisted until the flow was no longer quasi-geostrophic ($Q \ll 1$ and thus $Ro \sim 1$) and underwent a Kelvin–Helmholtz type of instability at the interface near the sidewall. For $F \geqslant 11$, however, there were transitions, as Q was decreased at constant F, to periodic amplitude vacillation and eventually to chaos. We define a chaotic signal as one which is aperiodic and displays a broadband Fourier spectrum. We will use the term 'noisy periodicity' to indicate a signal that appears nearly periodic but whose amplitude is modulated slightly with a chaotic component (Lorenz 1980), yielding a Fourier spectrum with sharp peaks but a relatively high 'noise' level. The route to chaos was observed to be via period-doubling, though some drifting of the period-doubled signals was observed in the experiment. In addition, the highest periodic solution observed before the onset of chaotic behaviour was a period-4 oscillation. It is unknown (*a*) whether the drifting was due to a quasi-periodic phenomenon or to experimental noise, and (*b*) whether the period-doubling cascade was incomplete or complete but unobservable experimentally.

The laboratory results for $\omega < 0$ (counter-rotating) showed interesting differences when compared to the $\omega > 0$ (co-rotating) case. For $Q < 0$, the axisymmetric basic state was significantly more stable than the $Q > 0$ case. For small negative values of Q, a steady travelling-wave solution was reached, but no time-dependent behaviour was observed in the parameter range studied. From figure 7, it is evident that differences exist for $|Q|$ values as large as 0.1, which corresponds to $Ro \approx 0.03$. The quasi-geostrophic f-plane model is invariant to changes in the sign of ω_T (or Q). The flow structure remains the same, only the direction changes. Thus, quasi-geostrophic models cannot capture the asymmetries in figure 7. Following the linear results, we

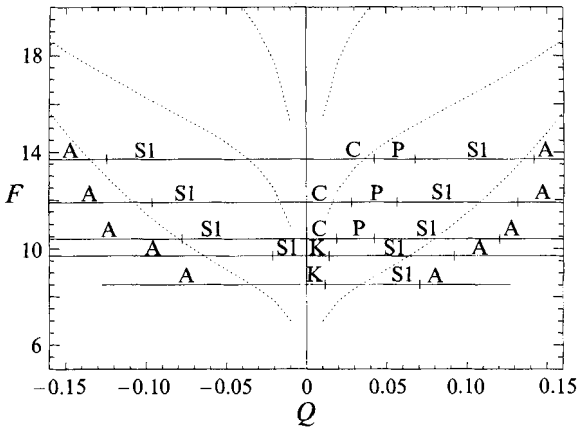

FIGURE 6. Experimental results on the f-plane. The dotted lines show the rigid-wall neutral curves for $k = 1, 2, 3$. A = axisymmetric basic-state solution, S1 = steady waves dominated by $k = 1$, P = periodic amplitude vacillation, C = chaos, K = Kelvin–Helmholtz instability (data from Hart 1985).

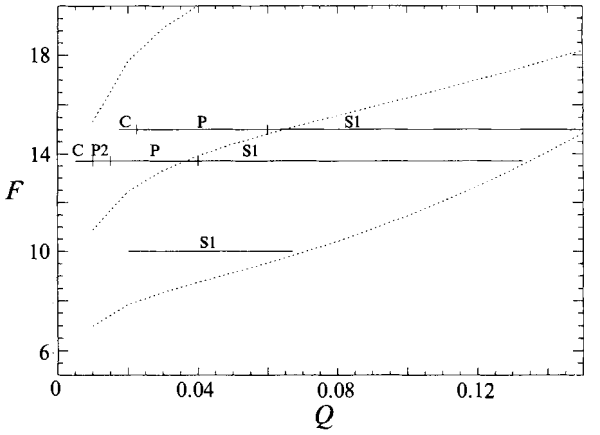

FIGURE 7. Numerical results on the f-plane. The dotted lines show the rigid-wall neutral curves for $k = 1, 2, 3$. S1 = steady waves dominated by $k = 1$, P = periodic amplitude vacillation, P2 = period-doubled amplitude vacillation with possible quasi-periodic modulation, C = chaos.

expect the dynamics of the quasi-geostrophic computations to be more complex than the results seen for $Q < 0$ and less complex than those found for $Q > 0$.

The numerical model was integrated over the experimental range of Q, and for Froude numbers $F = 10$, 13.7 and 15. The results are displayed in figure 7. We will refer to a mode composed of azimuthal wavenumber k and radial wavenumber m as mode (k, m). In agreement with experiment, at $F = 10$ the model exhibits a steady solution dominated by a wave with azimuthal and radial wavenumbers of 1 (i.e. mode (1,1)) over the entire range of Q studied. At $F = 13.7$, the solution is steady and primarily composed of the wave (1,1) when $Q > 0.04$. At $Q = 0.04$, the flow enters a regime of periodic amplitude vacillation (PAV); spatially, however, most of the energy still remains in the (1,1) mode. For $Q = 0.03$, PAV also exists, but the vacillation is somewhat different than that observed at $Q = 0.04$ (e.g. smaller wave amplitude, less variability in energy transfers). As Q is decreased to 0.015, the PAV solution bifurcates to a period-2 vacillation. The contribution of the (2,1) wave to

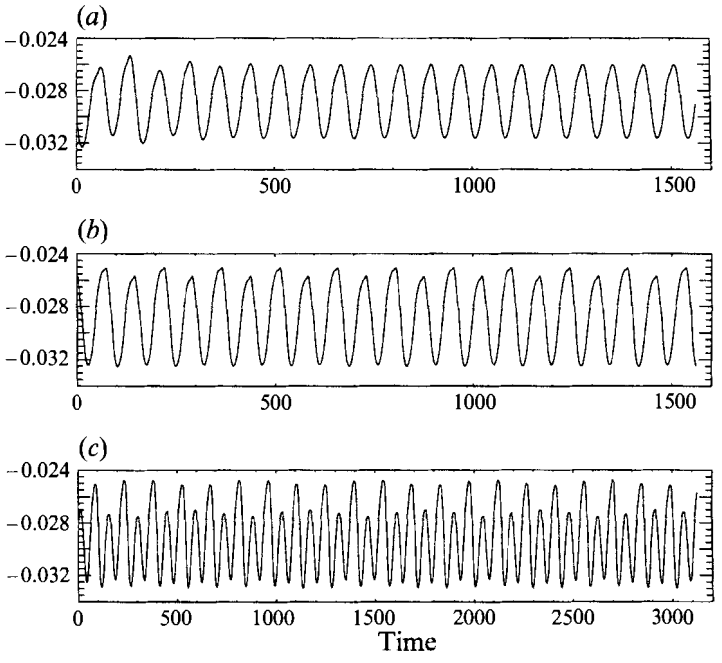

FIGURE 8. Time traces of baroclinic axis signal for $F = 13.7$. (*a*) $Q = 0.0175$ (PAV), (*b*) $Q = 0.015$ (period-2), (*c*) $Q = 0.012$ (modulated period-2).

the flow simultaneously becomes more visible, and throughout portions of the cycle, the (1,1) and (2,1) components possess roughly the same energy. When Q is further decreased to $Q = 0.012$, a low-frequency, small-amplitude signal begins to modulate the period-2 solution. This oscillation nearly phase locks at a frequency $1/8$ that of the predominant PAV period, causing the solution to look very much like a noisy period-8 vacillation. As Q is decreased to 0.011, the solution suddenly turns to PAV again, with both the period-doubling and the quasi-periodic modulation disappearing simultaneously. Finally, for $Q = 0.01$, the solution is chaotic. Figure 8 shows the baroclinic axis signal, i.e. P_{bc} at $r = 0$, for the PAV, period-2, and modulated period-2 (approximate period-8) regimes. At the axis, the contribution to the signal comes only from the zonal flow since the waves have zero amplitude at the origin, effectively filtering out the high-frequency travelling-wave signal. In this and all subsequent figures, the time scale is non-dimensional, so that the lid rotates in 2π time units.

The behaviour at $F = 13.7$ is consistent with the experimental observations in that there is a partial period-doubling cascade that appears to be somewhat 'noisy'. However, for small Q the numerical solution possesses narrow periodic windows while the experiment shows chaos. Moreover, the transitions to periodic and chaotic flow in the experiment occur at slightly larger values of Q than in the numerical results. Nonetheless, the qualitative agreement with experiment in the periodic regime is quite good, as both the numerical and laboratory PAV solutions oscillate with a period of approximately 12 lid periods, and the laboratory flow is also dominated by the wavenumber-1 component. Therefore, while the basic vacillation mechanism appears to be the same (corroborated by the excellent agreement in PAV periods), ageostrophic effects in the co-rotating laboratory experiments seem to destabilize the flow and hasten the transition to chaos.

For $F = 15$, the computed transition sequence is somewhat different than that

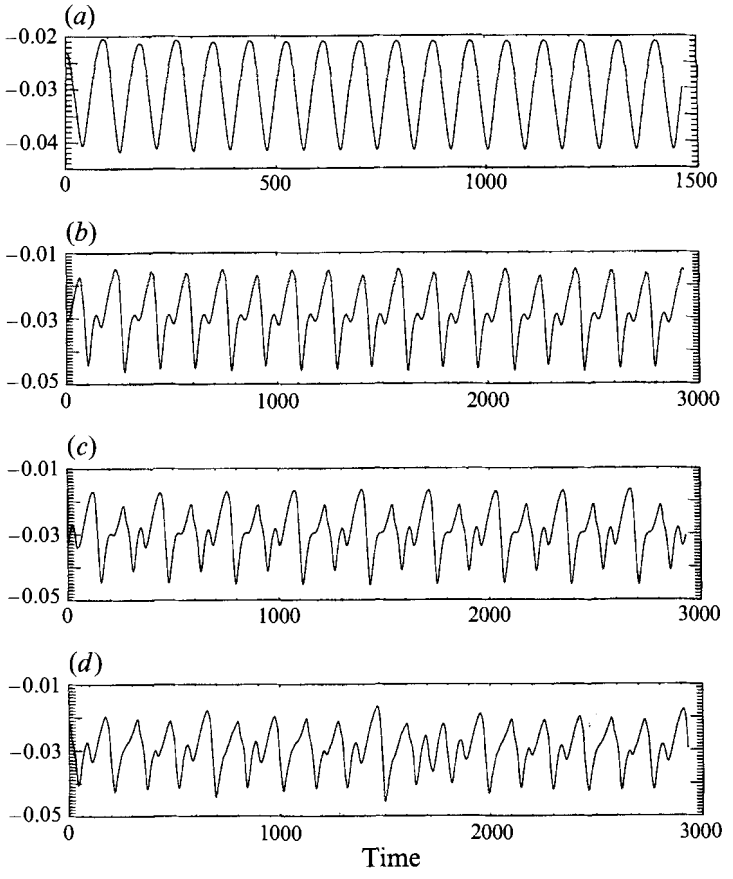

FIGURE 9. Time traces of baroclinic axis signal for $F = 15$. (*a*) $Q = 0.03$ (PAV), (*b*) $Q = 0.0225$ (noisy period-2), (*c*) $Q = 0.020$ (noisy period-4), (*d*) $Q = 0.0175$ (chaos).

observed at $F = 13.7$. Steady flow exists for $Q \geqslant 0.06$, and the system exhibits PAV in the region $0.0225 < Q < 0.06$. At $Q = 0.0225$, there is a long period of transient behaviour in which the system appears to reach a stable period-2 solution, but it eventually approaches an asymptotic state dominated by a period twice that in the PAV regime. In addition, the period-'doubled' signal appears to be modulated quasi-periodically with a period about 3 times the 'doubled' period (or 6 times the original PAV period), yielding a noisy period-2 solution. As Q is made smaller, the noisy period-2 solution bifurcates to a noisy period-4 signal, and further decreases in Q drive the system to a fully chaotic state. All of the solutions are dominated by the (1,1) wave with a small contribution from the (2,1) mode. Figure 9 shows the baroclinic axis signal in the periodic, noisy period-2, noisy period-4, and fully chaotic regimes. We note that the dominant period of the periodic solution at $Q = 0.03$ is half that of the other time series. The noisy period-doubling cascade is also consistent with the experimental results obtained at $F = 13.7$, but the main discrepancy is that the laboratory signal maintains the original PAV period as its primary vacillation period (instead of the doubled period).

5.3. *β-plane results*

In β-plane laboratory experiments, Ohlsen & Hart (1989*a*,*b*) found a rich spectrum of dynamical behaviour. Figure 10 summarizes the laboratory results for both co-

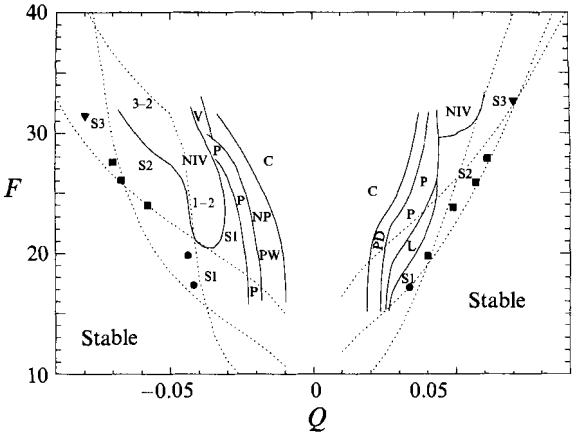

FIGURE 10. Experimental results on the β-plane. The dotted lines show the rigid-wall neutral curves for $k = 1, 2, 3$. Sn = steady waves with azimuthal wavenumber n, P = periodic amplitude vacillation, C = chaos, NIV = nonlinear interference vacillation, L = locked steady waves, NP = noisy periodicity, PW = periodic windows, V = narrow region of wavenumber vacillation. The circles, squares, and triangles are the same as in figure 4 (data from Ohlsen & Hart 1989*a*).

rotating and counter-rotating lid driving. Consistent with previous findings (Hart 1981; Pedlosky 1981), a general tendency for the dominant zonal wavenumber k to decrease with decreasing $|Q|$ (at constant F) was observed. Although in f-plane weakly nonlinear theory, Hart (1981) showed that only one wave can stabilize to finite amplitude, Mansbridge (1984) showed that on the β-plane a mixed-wave state is possible if β is large enough. For both co- and counter-rotating forcing, the experiments met the β criterion and mixed-wave states between wavenumber pairs 1,2 and 2,3 were observed.

In the co-rotating case ($Q > 0$), the transition sequence, as Q was decreased from the linear critical value, was largely the same for $15 < F < 30$. For a fixed value of F, the axisymmetric state yielded to a steady-wave solution just inside the neutral curve. For slightly smaller Q values, a travelling but phase-locked steady-wave state involving wavenumbers $k = 1$ and $k = 2$ occurred. As Q was decreased further, periodic amplitude vacillation appeared. This solution period doubled and eventually became chaotic as the lid driving was intensified. Finally, although the solutions for $Q > 0$ generally exhibited phase-locked waves, there also existed a region for $F \geqslant 30$ where nonlinear interference vacillation (NIV) was observed between wavenumbers 2 and 3. NIV (Ohlsen & Hart 1989*b*) is a phenomenon whereby two steady-amplitude waves travelling at slightly different speeds generate a time-periodic zonal flow correction via higher-order sideband interactions rather than through their direct interaction, which does not project onto the zonally averaged field.

The observed behaviour in the counter-rotating case was quite different than its co-rotating counterpart. Just inside the linear neutral curves, steady travelling-wave solutions with varying wavenumbers (depending on F) were observed. The most striking feature for $Q < 0$ was the large window of NIV observed for $F \geqslant 20$ and moderate values of Q. Depending on F, the NIV involved wavenumbers 1 and 2 or 2 and 3. As the lid driving was increased (i.e. $|Q|$ decreased), the interference vacillation yielded to a PAV solution, though for lower F the two were separated by a window of steady waves. The PAV solution was eventually supplanted by a noisy periodic

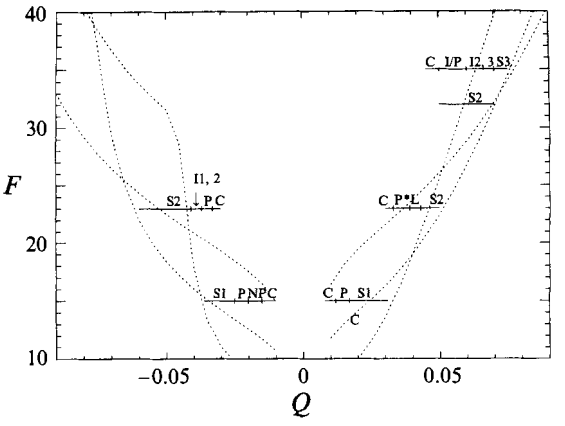

FIGURE 11. Numerical results on the β-plane. The dotted lines show the rigid-wall neutral curves for $k = 1, 2, 3$. Sn = steady waves with azimuthal wavenumber n, P = periodic amplitude vacillation, P* = periodic amplitude vacillation or period-doubled PAV, NP = noisy periodicity, C = chaos, In_1, n_2 = nonlinear interference vacillation with azimuthal wavenumbers n_1 and n_2, L = locked wave state between $k = 1$ and $k = 2$. The I/P notation at $F = 35$ indicates a small region where there exists either NIV or a phase-locked mixing of NIV and PAV in small windows.

solution and finally fully chaotic flow. For $F > 30$, a small window of wavenumber vacillation was also observed near $Q = -0.04$.

The numerical model was run at several values of F for both $Q > 0$ and $Q < 0$. Requirements on computational time prevented us from exploring the entire parameter space. Instead, values of F likely to yield the most representative behaviour were chosen, and the transition at these Froude numbers was explored in detail. The numerical results are summarized in figure 11.

For the co-rotating case at $F = 15$, the $k = 1$ wave is the most linearly unstable, and this is reflected in the dynamics. Just inside the neutral curve at $Q = 0.03$, a steady travelling-wave solution dominated by mode (1,1) exists. When Q is decreased to 0.017, the flow begins to exhibit PAV, but spatially the solution is still composed largely of the $k = 1$ component. This simple spatial dependence persists in the chaotic regime, which occurs abruptly (though with no observation of hysteresis) when Q is decreased below 0.012. The numerical solutions cannot be directly compared with experimental results since no laboratory data were taken for $F < 16.7$. However, no evidence of period doubling was found in the numerical model, which is observed in the laboratory data for somewhat larger values of F.

The solution at $F = 23$ is composed of a steady travelling wave with wavenumber 2 just inside the neutral curve. As Q is decreased to 0.043, the $k = 1$ wave grows to finite amplitude and a steady, mixed-wave state with $k = 1$ and $k = 2$ ensues. At $Q = 0.039$, this steady, phase-locked solution makes a transition to periodic amplitude vacillation. This solution period doubles and becomes fully chaotic for $Q \leqslant 0.033$. Time traces of the baroclinic axis signal are shown in figure 12 for the period-1, period-2, period-4, and chaotic solutions. In the periodic regime, the dominant PAV period is nearly the same (to within 5%) as that obtained from the laboratory experiment at comparable parameter values (cf. figure 15 of Ohlsen & Hart 1989*b*). The time series at $Q = 0.029$ appears more chaotic than that at $Q = 0.033$, near the onset of aperiodic behaviour. This increased temporal complexity at smaller Q was corroborated by return maps of successive minima of the time series, which show a nearly one-dimensional map for $Q = 0.033$ but a plane-filling attractor cross-section for $Q = 0.029$. Thus, the system

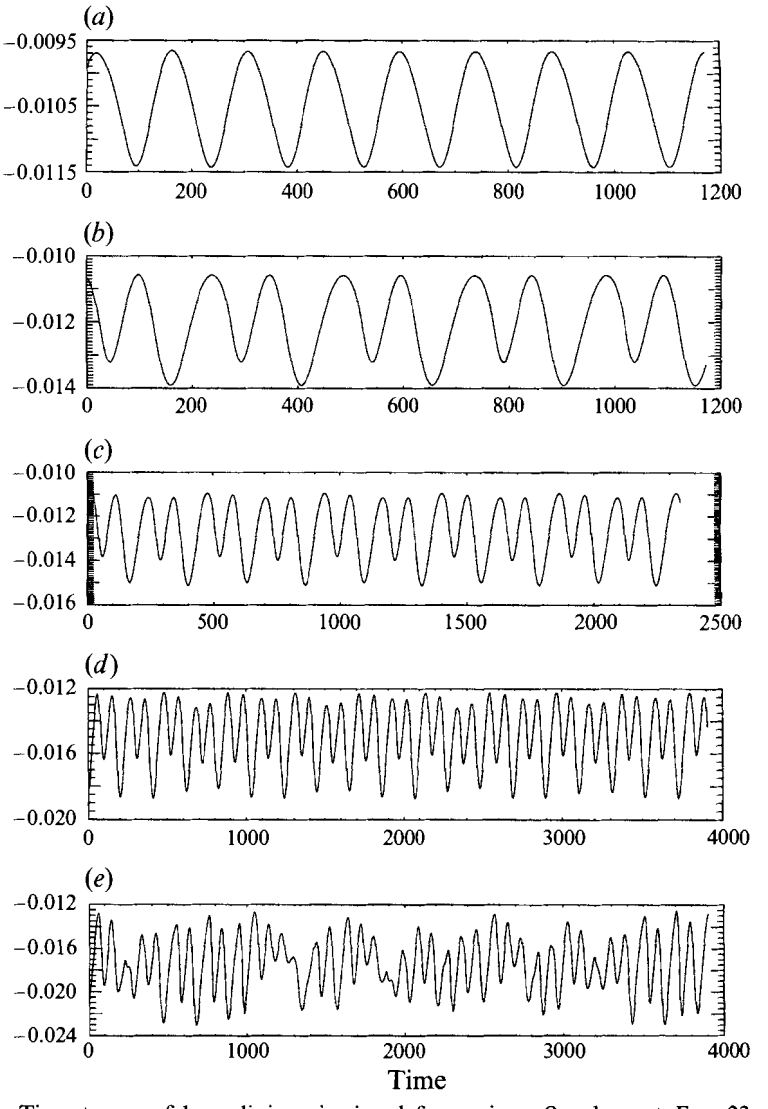

FIGURE 12. Time traces of baroclinic axis signal for various Q values at $F = 23$. (*a*) $Q = 0.039$ (period-1), (*b*) $Q = 0.037$ (period-2), (*c*) $Q = 0.036$ (period-4), (*d*) $Q = 0.033$ (chaos), (*e*) $Q = 0.029$ (chaos).

does not appear to stay low-dimensional over a wide range of parameter space. Once the system becomes chaotic, it becomes complicated somewhat rapidly, presumably owing to the presence of other instabilities.

At $F = 35$, there exists a mixed-wave NIV, rather than phase-locked, solution between wavenumbers 2 and 3. The NIV region is thus displaced upwards in the numerical model by about 10% in F compared to experiment, reflecting the larger (in F) crossover point between the $k = 2$ and $k = 3$ linear neutral curves. As Q is decreased further, the NIV mixes with a PAV-type solution and eventually becomes chaotic. The I/P region is a small window in Q where there is either NIV or a phase-locked mix of NIV and PAV.

In the counter-rotating case, the flow at $F = 15$ first exhibits a steady-wave state dominated by $k = 1$. As $|Q|$ is decreased, there is a transition first to PAV, then to

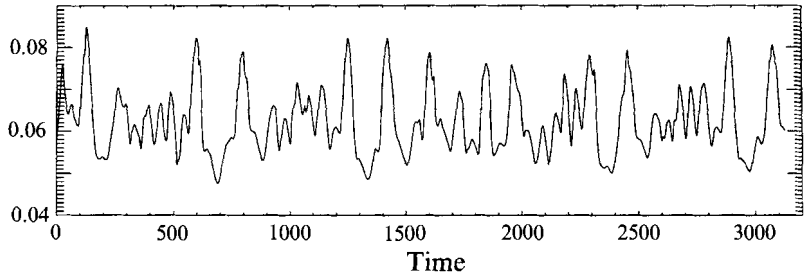

FIGURE 13. Time trace of axis interface height for $F = 23$, $Q = -0.033$. The contribution of both PAV and NIV behaviour to the overall signal is visible.

a noisy periodic solution, and finally to a fully chaotic state. This transition is very similar to that observed in the laboratory for $F = 16.7$ (cf. figures 3,4 from Ohlsen & Hart 1989*a*).

The counter-rotating solution at $F = 23$ exhibits a steady wavenumber-2 solution just inside the neutral curve at $Q = -0.045$. This yields to an NIV solution at $Q = -0.041$. Denoting the dominant frequencies of the $k = 1$ and $k = 2$ waves by f_1 and f_2, respectively, the zonal flow is observed to oscillate with a frequency $2f_1 - f_2$, a characteristic signature of nonlinear interference vacillation. This occurs because the primary interaction between the two waves does not alter the zonal flow. Instead, it produces another $k = 1$ wave with a higher radial structure and a frequency $f_1 - f_2$. This sideband then interacts with the original $k = 1$ wave to produce a zonal flow correction that oscillates with frequency $2f_1 - f_2$. In the experiment, Ohlsen & Hart (1989*b*) find that $f_1 \approx 0.113$, $f_2 \approx 0.197$, and the zonal flow vacillation period is about 5.5 lid periods. The numerical results yield $f_1 \approx 0.115$, $f_2 \approx 0.206$, and a zonal flow vacillation period of approximately 6.2 lid periods.

As $|Q|$ is decreased to $Q = -0.037$, the NIV is seemingly replaced by a PAV solution. In fact, the $k = 1$ and $k = 2$ waves do not become phase-locked as they do for amplitude vacillation when $Q > 0$. Instead, the PAV frequency is exactly half that of the NIV solution, and the dynamics are dominated by the much larger amplitude vacillation signal. When $|Q|$ is decreased further to $Q = -0.033$, the two secondary instabilities no longer remain phase-locked, and the solution then becomes chaotic. Figure 13 displays the axis interface height versus time at this parameter setting. The longer-period, large-amplitude signal is associated with a PAV vacillation, while the higher-frequency, smaller-scale component corresponds to the NIV behaviour.

The model results indicate that the NIV is inherently a nonlinear phenomenon. A calculation of linear phase speeds of the appropriate waves using the linear model presented in §4 does *not* indicate which solutions will be phase locked and which will not. In fact, all the linear phase speed ratios are typically non-integer by about 5%. By examining the phase speeds in the nonlinear model results, it is apparent that in the phase-locked case at $F = 23$, $Q > 0$, the $k = 1$ wave is already locked in phase with the steady $k = 2$ solution when it begins to grow. In contrast, in the two NIV regions, the second wave is out of phase with the steady solution even when the former is still very small. We thus conclude that the NIV and phase-locked solutions originate as secondary instabilities of the initial steady-wave solution. The six-wave, $E_{L_i} = 0$ model of Ohlsen & Hart (1989*b*) correctly reproduced the NIV for negative lid driving, which is not surprising given the similarity of the neutral curves in the two cases (see figure 4*b*). However, their model was unable to produce the phase-locking for positive lid driving, implying that either many spatial modes and/or

the no-slip boundary condition are required in order to produce the correct dynamics. As we argue in §6, the spatial behaviour in these regimes appears to be rather simple regardless of the sign of Q, indicating that the sidewall boundary condition is critical in dictating the behaviour of the system.

6. Spatial behaviour and EOF dimension

For both the f-plane and β-plane geometries, the dynamics are spatially dominated by the $k = 1$ mode for relatively small values of F, where the gravest zonal harmonic is the most linearly unstable. However, for F large enough such that both zonal wavenumbers 1 and 2 are linearly unstable for relatively large $|Q|$, there is observed a tendency for strong wave–wave interactions, which subsequently give rise to complex dynamics such as wavenumber vacillation, NIV or chaos. One useful tool for understanding the salient spatio-temporal dynamics of the system is Karhunen–Loeve decomposition (Loeve 1955), by which we can obtain the empirical orthogonal functions (EOFs) of the flow. This method is described in detail by Sirovich (1989); briefly, it yields, using second-order statistics, the primary spatial structures involved in the dynamics. These are ordered according to their time-averaged projection onto the overall flow field. An EOF analysis thus reveals a measure of the number of independent modes that partake in the observed behaviour.

Mundt & Hart (1994) have previously applied this analysis to an f-plane, quasi-geostrophic model in a channel geometry with great success. They found that the dominant EOFs are equivalent in structure to the eigenfunctions of the secondary instabilities of the equilibrated, steady, baroclinic wave state. Each transition to a new temporal state is accompanied by the concomitant appearance of new spatial modes acting as a coherent oscillator. Moreover, these spatial modes act to break the symmetries of the channel geometry discussed in §2. In the channel, spatial and temporal behaviour are thus intimately intertwined and the transition to chaos is not well described by a low-order system such as a single wave model. We wish to determine whether the cylinder model, lacking these symmetries, behaves in a similar fashion. In this section, we apply EOF decomposition to both the f- and β-plane numerical results in order to both extract the inherent spatial complexity of the flow in different regimes, and also to address the role that symmetry breaking plays in the observed dynamics.

6.1. *f-plane*

To examine the spatial component of the transition to chaos on the f-plane, EOF decomposition was performed on the barotropic and baroclinic streamfunctions at $F = 13.7$ for $Q = 0.05$ (steady), $Q = 0.04$ (PAV), $Q = 0.03$ (PAV), $Q = 0.02$ (PAV), $Q = 0.015$ (period-2 PAV), $Q = 0.011$ (PAV), and $Q = 0.01$ (chaos). All of the numerical solutions presented in this study possess a fast time scale owing to the presence of travelling waves; the energy of the system, however, vacillates on a much longer time scale which is an order of magnitude larger than the reciprocal of the gravest wave phase frequency. Owing to computer memory limitations, this property of the solutions negates the possibility of obtaining extremely accurate EOF decompositions in chaotic regimes, since to ensure valid statistics it is generally necessary to sample over many slow-time vacillations while still resolving the fast time scale. However, a relatively small number of snapshots is often adequate to resolve the dominant EOFs, which comprise the large-scale structure of the flow.

At $Q = 0.05$, the steady wave fields are strongly dominated by mode (1,1) with

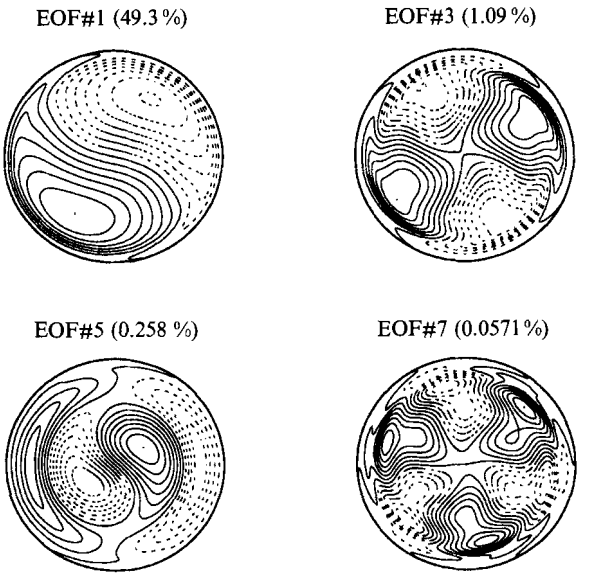

FIGURE 14. Odd EOFs of baroclinic wavy field for $Q = 0.04$ at $F = 13.7$ (periodic amplitude vacillation). The even EOFs, not shown, are nearly identical to their odd counterparts but are phase-shifted to maintain the orthogonality condition. The solid and dashed lines indicate positive and negative height anomalies, respectively.

a small contribution by (2,1) (in practice, the EOFs are generally not pure waves, but are nearly so for the solutions presented here). In the PAV regime at $Q = 0.04$, the barotropic and baroclinic wavy fields are composed, in order of decreasing contribution, of modes (1,1), (2,1), (1,2), and (3,1). The odd baroclinic wavy EOFs are shown in figure 14. The even EOFs, which are not shown, are nearly identical to their odd counterparts but are phase shifted to maintain orthogonality. The notation 'even' and 'odd' simply refers to the index of the EOFs when they are sorted from largest variance to smallest (i.e. the EOF with the largest variance is denoted as EOF #1, that with the second largest variance EOF #2, etc.). For all the fields to be presented, the solid and dashed lines respectively indicate positive and negative interface deviations. The percent variance captured by each mode, on average, is shown in parentheses. Overall, the first two baroclinic wavy EOFs capture 97% of the variance of their respective field. The effect of the rigid sidewall, which tends to retard the flow near $r = 1$, can be clearly seen.

For the slightly different PAV vacillation at $Q = 0.03$, the relatively insignificant (1,2) and (3,1) modes switch their order, but the dominant wave structures are unchanged. The first two baroclinic wavy modes now capture 95% of the variance, slightly less than at $Q = 0.04$. As Q is further decreased, the EOFs remain nearly the same but the variance possessed by the first two modes continues to decrease, until in the chaotic regime at $Q = 0.01$, the energy captured by the first two EOFs is about 88%.

EOF decomposition was also performed at $F = 15$ for $Q = 0.05$ (PAV), $Q = 0.03$ (PAV), $Q = 0.025$ (PAV), $Q = 0.0225$ (noisy period-2), and $Q = 0.0175$ (chaos). The spatial behaviour of all the PAV solutions is very similar to the amplitude vacillation observed at $F = 13.7$ and shows little variation with Q. Figure 15 shows the first four odd EOFs at $Q = 0.025$, just before the transition to the noisy period-2 regime. They are nearly identical to those shown in figure 14. Although the transition from

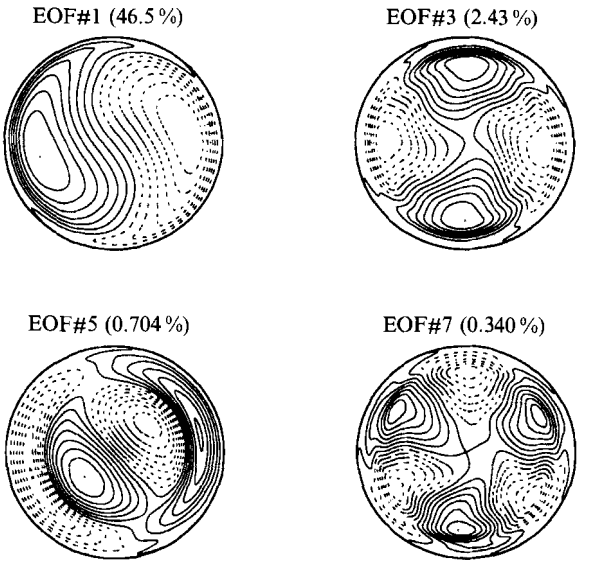

FIGURE 15. Odd EOFs of baroclinic wavy field for $Q = 0.025$ at $F = 15$ (periodic amplitude vacillation).

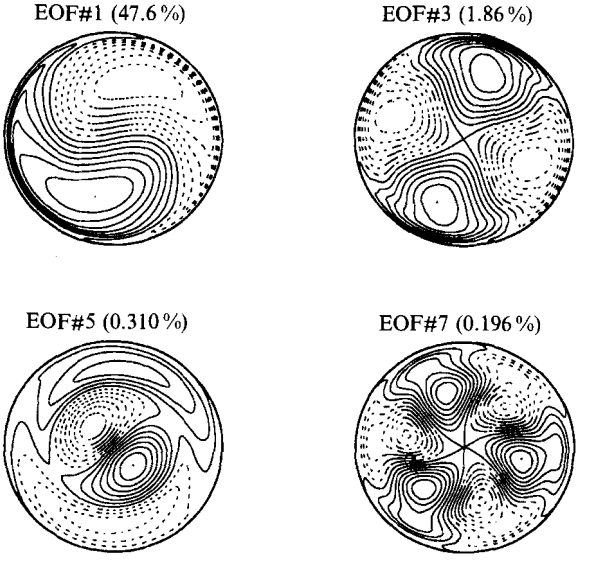

FIGURE 16. Odd EOFs of baroclinic wavy field for $Q = 0.015$ at $F = 15$ (periodic amplitude vacillation).

PAV to the noisy period-2 behaviour is accompanied by a significant increase in the variation of kinetic energy in the flow, the EOF spectra of the two solutions show no significant differences. The bifurcation sequence thus appears to be purely temporal.

6.2. *β-plane*

For the co-rotating case at $F = 15$, EOFs were computed at $Q = 0.015$ (PAV) and $Q = 0.012$ (chaos). For $Q = 0.015$, the first four odd baroclinic wavy EOFs are shown in figure 16. The (1,1) mode is dominant and the first pair of EOFs captures 95% of the variance. The dynamics are thus heavily influenced by the gravest zonal

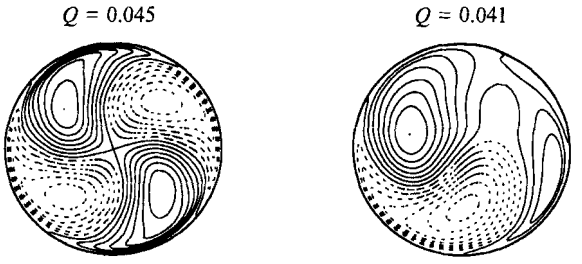

FIGURE 17. Baroclinic wavy field for $Q = 0.045$ (steady $k = 2$ solution) and $Q = 0.041$ (locked $k = 1, 2$ state) at $F = 23$.

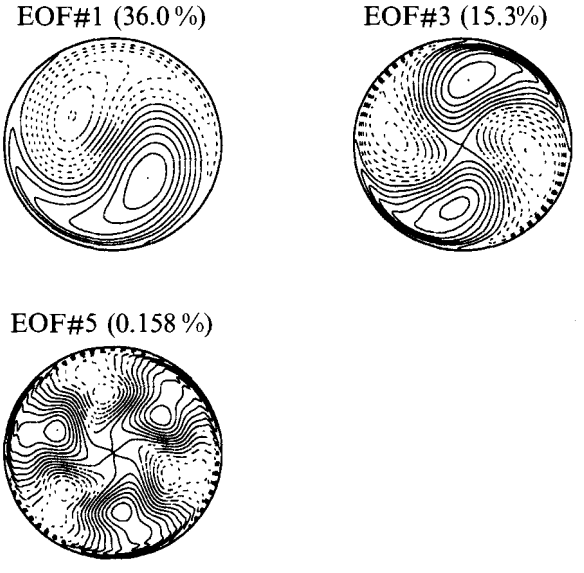

FIGURE 18. EOFs of baroclinic wavy field for $Q = 0.041$ at $F = 23$.

harmonic. In the chaotic regime at $Q = 0.012$, the EOFs are nearly identical to those at $Q = 0.015$. Similar to the f-plane findings, the transition to chaotic flow seems to be temporal and is not associated with a change in the spatial representation of the flow.

For the co-rotating case at $F = 23$, the baroclinic wavy field is shown in figure 17 for the steady $k = 2$ solution at $Q = 0.045$ and for the locked $k = 1, 2$ state at $Q = 0.041$. Figure 18 shows the baroclinic wavy field at $Q = 0.041$ when decomposed into EOFs; only the odd empirical functions are shown. The solution naturally separates into fields composed of a particular zonal wavenumber. The (1,1) mode dominates and captures about 70% of the variance, while the (2,1) wave captures nearly 30%. The (3,1) contribution is quite small and nets less than 0.5% of the total variance. Thus, the solution is essentially a linear combination of the (1,1) and (2,1) waves. Although the solution is actually a 'frozen' pattern travelling around the tank, the requirement of orthogonality necessitates two EOF pairs for adequate representation.

EOF decomposition was used to reveal the dominant spatial modes in the system in the period-1, period-2, period-4, and chaotic regimes at $F = 23$. Figure 19 displays the odd baroclinic wavy EOFs at $Q = 0.037$ in the period-2 regime. The first three pairs of EOFs contain nearly all the energy and are identical to the structures seen in

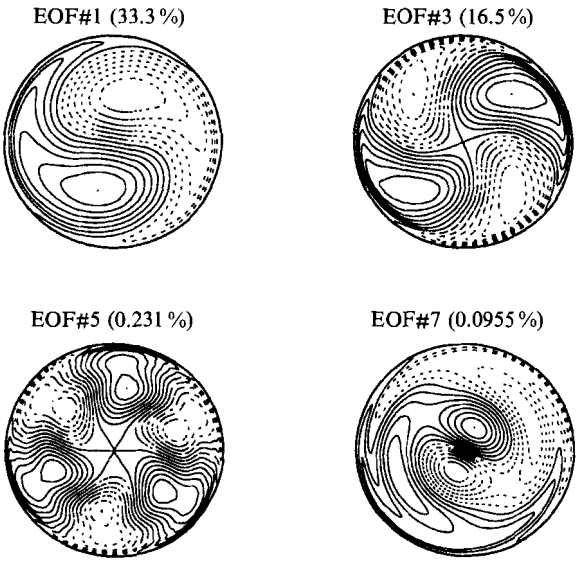

FIGURE 19. Odd EOFs of baroclinic wavy field for $Q = 0.037$ at $F = 23$ (period-2 amplitude vacillation).

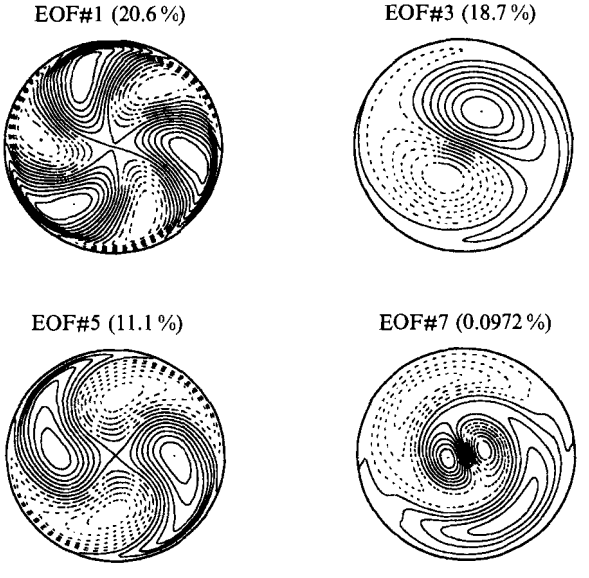

FIGURE 20. Odd EOFs of baroclinic wavy field for $Q = 0.065$ at $F = 35$ (NIV).

the locked state in figure 19. In fact, the EOF analysis indicates that the spatial modes do *not* change as the system period-doubles into chaos. The spatial structure of the EOFs is unaltered, and the percent variance captured by each mode is changed only slightly, with the lower-variance modes becoming more energetic as Q is decreased. The transition to chaos is again purely temporal.

EOFs were also obtained in the co-rotating case at $F = 35$, $Q = 0.065$, where NIV occurs between wavenumbers 2 and 3. Figure 20 displays the odd baroclinic wavy EOFs in this regime. Interestingly, the $k = 1$ sideband produced by the interaction of the two primary waves is itself larger than the (2,1) mode. Nonetheless, the EOF

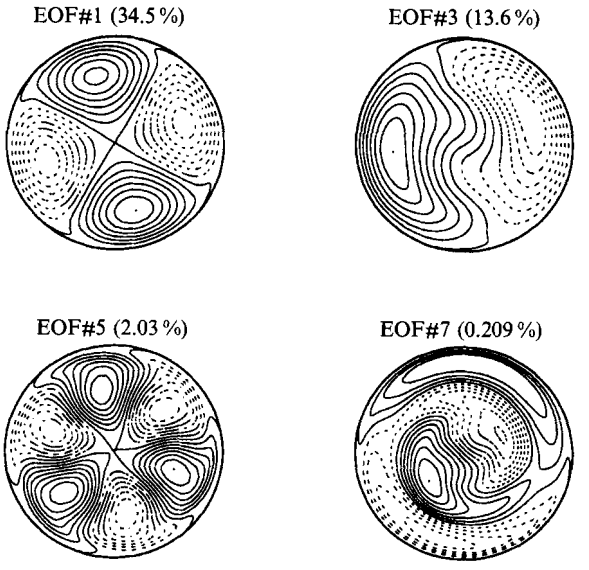

FIGURE 21. Odd EOFs of baroclinic wavy field for $Q = -0.039$ at $F = 23$ (NIV).

analysis confirms that the dynamics are governed by the two primary waves and the sideband resulting from the nonlinear interaction of the two, since the remaining EOFs possess a negligible amount of energy. Moreover, an examination of the associated time series of the $k = 1$ EOF indicates that it has a phase speed of $f_3 - f_2$, where f_2 and f_3 are the phase speeds of the $k = 2$ and $k = 3$ waves, respectively. In agreement with prediction (Ohlsen & Hart 1989*b*), the NIV solution possesses a vacillation frequency $2f_3 - 3f_2$.

In the counter-rotating case at $F = 15$, the behaviour is dominated by the (1,1) mode, similar to the f-plane and co-rotating β-plane results. This simple spatial dependence persists in the noisy-periodic and chaotic regimes, indicating yet again that the transition to chaos is largely temporal in nature. However, the dominance of the (1,1) mode decreases somewhat as the transition to chaos is made, and the lower-energy modes become more energetic, indicating that the nonlinearities are enhanced as $|Q|$ is decreased.

The spatial dependence of the NIV in the counter-rotating case appears quite different from the solution at $F = 35$, $Q > 0$. The odd EOFs of the baroclinic wavy field are displayed in figure 22 at $F = 23$ and $Q = -0.039$. In this situation, the (2,1) and (1,1) modes, which are the primary waves, comprise the first two pairs of EOFs. The sidebands (3,1) and (1,2), which arise from the nonlinear interactions of the two primary waves, form the next two pairs of empirical functions. The higher-order EOFs, which contribute a negligible portion of the overall energy, are composed of higher-wavenumber terms. The structure of the dominant EOFs is quite different from those observed in the co-rotating case (figure 20). The shearing due to the sidewall boundary layer is almost unnoticeable for $Q < 0$, and the EOFs resemble the linear eigenfunctions of the $E_{L_i} = 0$ problem. This may explain the success of low-order, $E_{L_i} = 0$ models in reproducing NIV for counter-rotating lid driving (Ohlsen & Hart 1989*b*). Interestingly, an EOF analysis in the PAV regime at $Q = -0.037$ reveals that the spatial mode shapes are unaltered. However, the first two pairs of EOFs are interchanged, with the $k = 1$ contribution becoming the dominant structure of the flow. The dominant EOFs in the chaotic regime at $Q = -0.033$ are

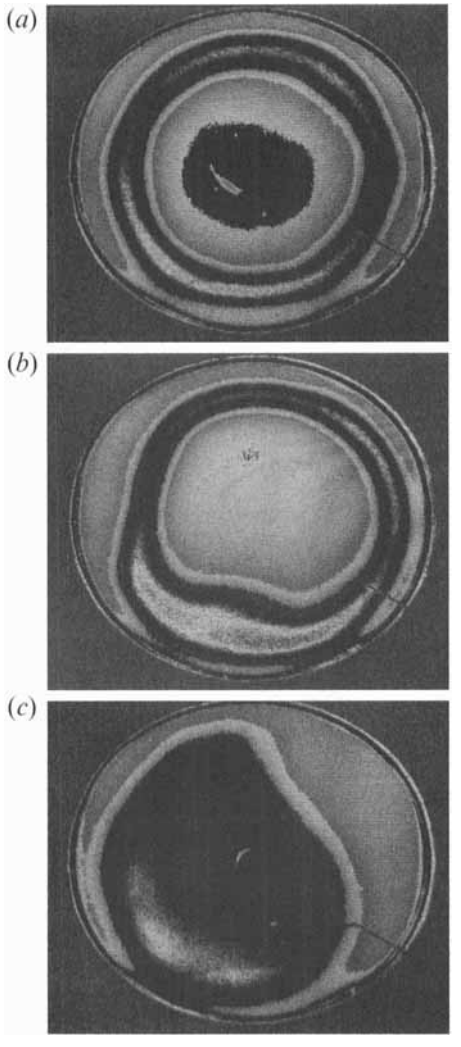

FIGURE 22. Snapshots of interface height shapes during the growth of an amplitude vacillation ($a \rightarrow c$) with flat topography for $F = 18$, $Q \approx 0.02$. The fluid properties and cylinder dimensions are similar to those cited in table 1.

nearly identical to those at $Q = -0.037$. Therefore, as with $Q > 0$, the transition to chaos is temporal. The NIV and PAV solutions involve the same spatial modes, but in differing proportions. Chaos likely ensues from a competition between these two possible states.

6.3. *Spatial structures in experiments*

One obvious characteristic of the computational simulations is the comma shape of the dominant lowest-order EOF (e.g. figures 16, 20 top left). It is interesting that computational simulations that omit lateral friction, and so have no lateral shear in the basic state near $r = 1$, do not predict 'comma clouds' such as these. For example, in the cylinder model of Yoshida & Hart (1986), which has a basic state of equal but opposite solid rotation all the way to the wall in the two layers, the interface height fields are nearly symmetric in azimuth about the ridges.

The laboratory experiments cited above were instrumented with two or three

interface height gauges. From these probes it is difficult to detect features such as those shown in figures 14–21, for example. However, polarimetry (Hart & Kittelman 1986) yields spatial structures very similar to the dominant EOFs. In this visualization method, the lower-layer fluid (usually water–alcohol) is replaced by an optically active liquid (Limonene). When the cylinder is illuminated with polarized light from below, the beam is rotated in proportion to the layer depth. If a camera looks down from above through a crossed polarizer, images of interface depth may be obtained directly. Figure 22 shows a typical example of the growth of a disturbance during a vacillation cycle for a co-rotating flow. The comma shape is obvious. The geometry for this lab experiment is slightly different from the computations in that the bottom and top surfaces are flat, but since the computations for both the f- and β-planes show comma shapes to be ubiquitous, we regard this as another confirmation that the essential physics of baroclinic chaos in a cylinder is being captured by the model.

7. Conclusions

We have formulated a high-resolution model of two-layer, quasi-geostrophic flow in a cylinder with rigid sidewalls. A calculation of the linear stability curves using the no-slip condition yields an improvement over previous theoretical implementations that ignore lateral friction. In the nonlinear regime, f-plane calculations generally show good agreement with experimental results, although the latter become chaotic at larger values of Q than the former. As anticipated, the computations exhibit behaviour that is somewhat the 'average' of that observed in the laboratory for $Q < 0$ and $Q > 0$. The lack of complete correspondence of our f-plane numerical results with experimental findings, and the behaviour of the laboratory flow itself, indicates that higher-order effects are important even when $|Q|$ is relatively large and hence Ro is small. The inclusion of ageostrophic terms is a logical extension of this study, and accounting for such effects will hopefully mitigate the remaining discrepancies between computational simulations and laboratory experiment. On the β-plane, results for both co-rotating and counter-rotating lid driving show excellent agreement with experiment. It is unclear why the β-plane laboratory behaviour is more faithful to the quasi-geostrophic numerical simulations than its f-plane counterpart. The computations reveal that when $\beta \neq 0$, the $k = 1$ and $k = 2$ waves have approximately equal amplitudes. On the f-plane, however, the $k = 1$ wave is dominant. Perhaps on the β-plane the interaction between the first two zonal harmonics (which is integral in generating the observed chaotic behaviour) obviates the importance of the shear layer at the sidewall, where the flow is most ageostrophic.

The present study indicates that the behaviour in a cylindrical geometry depends crucially on the sidewall boundary conditions, a phenomenon which has already been observed in the channel (Mundt *et al.* 1995). For example, previous calculations (Ohlsen & Hart 1989*b*) using a moderately resolved β-plane model with $E_{L_i} = 0$ yield NIV for both signs of lid driving instead of phase-locking for $Q > 0$, as found in this study. The computational simulations reveal that, in the NIV regime on the β-plane ($Q = -0.039$), the region of large vorticity and vorticity gradient for the waves is confined to the outer 3% of the domain. The confinement of the effect of the no-slip sidewall explains the success of the afore-mentioned model when $Q < 0$. However, for both the f-plane and the co-rotating β-plane cases, the wavy fields have large values of vorticity in the outer 15% of the domain. Thus, the presence of the viscous sidewall boundary layer generally appears to have a global effect on the dynamics, and its inclusion is essential for accurately simulating the laboratory flows.

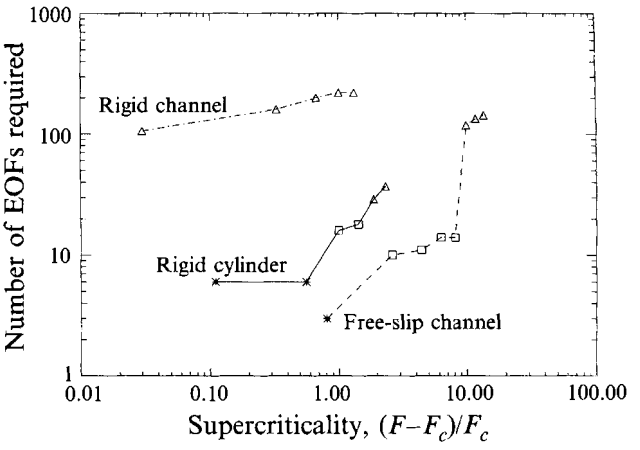

FIGURE 23. Number of EOFs required to meet 99% variance threshold versus supercriticality for rigid cylinder model, rigid channel model, and free-slip channel model. Steady, periodic, and chaotic behaviour are respectively indicated by asterisks, squares, and triangles.

For both f-plane and β-plane scenarios, the transition to chaos is largely temporal. In all of the cases studied, the chaotic behaviour is observed to have the same dominant spatial structures as the less complex (e.g. periodic) regimes in a nearby region of parameter space. This is in sharp contrast to the behaviour observed in computer simulations of zonally periodic channel flow, where chaos is achieved by the emergence of many interacting instabilities, each with its own unique spatial signature and temporal frequency. The shift-reflect and flip-reverse symmetries present in the channel (and which manifest themselves in these instabilities) owe their existence to the particular geometry and choice of physical parameters; the cylinder geometry lacks the former symmetry, and the experimental setup (i.e. $\chi \neq 1$, $\bar{v}_{bt} \neq 0$, $\beta \neq 0$) eliminates the latter.

In the rigid cylinder, the number of EOFs needed to represent the spatio-temporal dynamics in the chaotic regime is generally far less than the number required in both rigid and free-slip channels. Figure 23 shows the number of EOFs required to meet a 99% variance threshold versus the supercriticality $(F-F_c)/F_c$ (where F_c is the critical value of F required for linear instability) for three cases: rigid cylinder, rigid channel, and free-slip channel. The computations were performed on the f-plane at $Q = 0.05$. The Ekman numbers used are the same as in §5.2. For these parameter settings, the rigid channel is subcritically chaotic, and approximately 100 modes are needed to capture the dynamics near $F = F_c$. As the supercriticality is increased, the required number of EOFs increases to about 200. In the free-slip channel, the onset of chaos does not occur until the supercriticality is about 10, but again around 100 EOFs are needed to represent the dynamics faithfully. In contrast, the rigid cylinder begins to exhibit chaotic behaviour when the supercriticality is about 1.5 (consistent with laboratory experiments), and only about 35 EOFs are necessary to meet the variance threshold. The findings of this study therefore suggest, somewhat counter-intuitively, that the elimination of symmetries actually simplifies the spatial dynamics, possibly by reducing the number of possible 'sub-states' in which the solution can dwell, and hence eliminating potential competition between these sub-states.

The idea, which remains to be investigated in more detail, is that the zonal channel has two active symmetries. As shown in Mundt & Hart (1994), this leads to four independent symmetry-breaking secondary instabilities of the steady equilibrated

baroclinic wave system. The secondary instabilities are weakly coupled, have vastly different spatial structures (again obeying or lacking certain symmetries), and have incommensurate frequencies. This situation appears to be central to the quasi-periodic flow observed on the road to chaos in the symmetric geometry, where at finite amplitude mixed secondary instability states will be characterized by two or more unrelated frequencies. In addition, the number of secondary instabilities grows rapidly with supercriticality, accounting, probably, for the rapid dimension increase in the free-slip and rigid channels. In the cylinder, as we have shown, the fundamental wave pattern is asymmetric (essentially just the comma mode), and this pattern is dominant throughout the transition region. The geometric asymmetry seems to collapse the multiple instabilities of the channel into one mode, and hence the resulting vacillating and chaotic states are of lower dimension. Although the cylinder with top-only forcing may appear more complex in its geometry and basic states than the nicely symmetric zonal channel, the dynamics contained within it is simpler! As many objects (spherical shell atmospheres, ocean basins, etc.) studied in geophysical fluid dynamics are more akin to the cylinder, this observation, if verified by studying more examples as well as the basic theory for bifurcations in symmetric and asymmetric systems, may be significant.

This research was supported by the National Science Foundation under grant ATM-9025087. Computational resources were provided in part by NASA grant NAG8-190 and contract NAS8-31958. We are most grateful to these sponsors.

Appendix

The coefficients for the basic-state solution shown in (3.1),(3.2) are as follows:

$$\gamma_{1,2} = \frac{(\chi-1)(\chi+1)}{\chi^2} \mp \frac{1}{\chi^2}(\chi^4 - \chi^2 + 1)^{1/2}, \tag{A 1}$$

$$\lambda_{1,2} = \left(\frac{|Q|}{E_1/Ro}\right)^{1/2} \left[\frac{2\chi + 1 - \chi\gamma_{1,2}}{\chi+1}\right]^{1/2}, \tag{A 2}$$

$$c_1 = -\frac{[\gamma_2(\chi+2)-1]}{2(\chi+1)(\gamma_2-\gamma_1)I_1(\lambda_1)}, \tag{A 3}$$

and

$$c_2 = -\frac{[\gamma_1(\chi+2)-1]}{2(\chi+1)(\gamma_1-\gamma_2)I_1(\lambda_2)}. \tag{A 4}$$

If $\chi = 1$, these reduce to

$$\gamma_{1,2} = \mp 1, \tag{A 5}$$

$$\lambda_1 = \left(\frac{2|Q|}{E_1/Ro}\right)^{1/2}, \tag{A 6}$$

$$\lambda_2 = \left(\frac{|Q|}{E_1/Ro}\right)^{1/2}, \tag{A 7}$$

$$c_1 = -\frac{1}{4I_1(\lambda_1)}, \tag{A 8}$$

and

$$c_2 = -\frac{1}{2I_1(\lambda_2)}. \tag{A 9}$$

REFERENCES

ANDERSON, D. A., TANNEHILL, J. C. & PLETCHER, R. H. 1984 *Computational Fluid Mechanics and Heat Transfer*. Hemisphere.

CANUTO, C., HUSSAINI, M. Y., QUARTERONI, A. & ZANG, T. A. 1988 *Spectral Methods in Fluid Dynamics*. Springer.

CATTANEO, F. & HART, J. E. 1990 Multiple states for quasi-geostrophic channel flows. *Geophys. Astrophys. Fluid Dyn.* **54**, 1–33.

HART, J. E. 1972 A laboratory study of baroclinic instability. *Geophys. Fluid Dyn.* **3**, 181–209.

HART, J. E. 1981 Wavenumber selection in nonlinear baroclinic instability. *J. Atmos. Sci.* **38**, 400–408.

HART, J. E. 1985 A laboratory study of baroclinic chaos on the f-plane. *Tellus* **37A**, 286–296.

HART, J. E. 1986 A model for the transition to baroclinic chaos. *Physica D* **20**, 350–362.

HART, J. E. & S. KITTELMAN 1986 A method for measuring interfacial fields in the laboratory. *Geophys. Astrophys. Fluid Dyn.* **36**, 179–185.

KLEIN, P. & J. PEDLOSKY 1986 A numerical study of baroclinic instability at large supercriticality. *J. Atmos. Sci.* **43**, 1243–1262.

LOEVE, M. M. 1955 *Probability Theory*. van Nostrand.

LORENZ, E. N. 1980 Noisy periodicity and reverse bifurcation. *Ann. NY Acad. Sci.* **357**, 282–291.

MANSBRIDGE, J. V. 1984 Wavenumber transition in baroclinically unstable flows. *J. Atmos. Sci.* **41**, 925–930.

MUNDT, M. & HART, J. E. 1994 Secondary instability, EOF reduction, and the transition to baroclinic chaos. *Physica D* **78**, 65–92.

MUNDT, M., BRUMMELL, N. H. & HART, J. E. 1995 Linear and nonlinear baroclinic instability with rigid sidewalls. *J. Fluid Mech.* **291**, 109–138.

OHLSEN, D. R. & HART, J. E. 1989*a* The transition to baroclinic chaos on the β-plane. *J. Fluid Mech.* **203**, 23–50.

OHLSEN, D. R. & HART, J. E. 1989*b* Nonlinear interference vacillation. *Geophys. Astrophys. Fluid Dyn.* **45**, 215–235.

PEDLOSKY, J. & FRENZEN, C. 1980 Chaotic and periodic behaviour of finite-amplitude baroclinic waves. *J. Atmos. Sci.* **37**, 1177–1196.

PEDLOSKY, J. 1981 The nonlinear dynamics of baroclinic wave ensembles. *J. Fluid Mech.* **102**, 169–209.

QUARTAPELLE, L. & VALZ-GRIS, F. 1981 Projection conditions on the vorticity in viscous incompressible flows. *Intl J. Numer. Meth. Fluids* **1**, 129–144.

SIROVICH, L. 1989 Chaotic dynamics of coherent structures. *Physica D* **37**, 126–145.

STEWARTSON, K. 1957 On almost rigid rotations. *J. Fluid Mech.* **3**, 17–26.

YOSHIDA, A. & HART, J. E. 1986 A numerical study of baroclinic chaos. *Geophys. Astrophys. Fluid Dyn.* **37**, 1–56.